Soils and Rocks
www.soilsandrocks.com
An International Journal of Geotechnical and Geoenvironmental Engineering
ISSN 1980-9743
ISSN-e 2675-5475

Microstructural characterization of a 3D-printed soil

Alessio Ferrari[1,2], Marco Rosone[1], Silvia La Rosa[1], Giovanni Sapienza[1]

Article

Keywords
3D-printing
Soil additive manufacturing
Soil extrusion
Soil fabric

Abstract

Transversal applications of 3D-printing (or Additive Manufacturing) have been recently implemented in the field of Geomechanics. In a 3D-printing process, the printed volume is obtained from successive layering of adjacent soil filaments. In this work, the fabric of an as-printed soil has been carried out by combining Mercury Intrusion Porosimetry (*MIP*) tests and Scanning Electron Microscope (*SEM*) observations, with the aim to highlight how the particle arrangements and the orientation and shape of pores are linked to the printing operation. The microstructural analyses showed that macropores are the result of the relative position of the filaments and their initial distortion in quasi-undrained conditions. Particle arrangement within the soil filament is strongly anisotropic, due to the rotative movement of the soil in the extruder.

1. Introduction

The fields of application of 3D-printing (or Additive Manufacturing) are constantly growing, including uses in Geomechanics. 3D-printing of polymeric materials has been used to manufacture synthetic porous samples aiming at mimicking characteristics of soils and rocks (Ju et al., 2014; Dal Ferro & Morari, 2015; Bourke et al, 2016; Gomez at al., 2019). On the other hand, soils have been also used as printing materials, for artistic scopes, for the preparation of samples for laboratory testing (Hanaor et al., 2015; Matsumura & Mizutani, 2015; Mansoori et al., 2018; Pua et al., 2018; Pua & Caicedo, 2020), or even for the construction of structures and infrastructures (Khoshnevis, 2004; Perrot et al., 2018).

In a printing process, the soil exits from the printer as filaments along prescribed paths; the result is a volume consisting of successive layers of adjacent soil filaments. The fabric of the printed soil is then the result of the initial microstructural characteristics of the filament, of the relative position of the adjacent filaments, and of all possible hydro-mechanical loads happening in the process (e.g increase of total stress as the layers overlap, or variations in water content due to exposure to hygroscopic conditions).

There is strong evidence on the fundamental role of the fabric of clayey soils on their hydro-mechanical response (e.g. Romero & Simms, 2008; Muñoz-Castelblanco et al., 2012; Cordão Neto et al., 2018; Ferrari et al., 2022). This link seems highly relevant for a 3D-printed soil, in which the fabric can be seen as a controlled result of the printing process. In this regard, this note presents the results of a microstructural investigation carried out on 3D-printed soil samples prepared with a commercial 3D-printer, specifically adapted to be used with a fine soil. The different microstructural peculiarities of the as-printed samples are identified and discussed thanks to the combined use of Scanning Electron Microscope (*SEM*) and Mercury Intrusion Porosimetry (*MIP*).

2. Material and methods

A commercial clayey soil used for artistic purposes was used as printing material; the geotechnical characteristics are listed in Table 1. Starting from the as-received condition, the soil was accurately mixed with distilled water to reach a consistency index *CI* close to 0.5 (corresponding target water content $w = 0.32$), which ensured adequate workability and limited the occlusion of air bubbles in the soil during the printing process.

A *Delta-WASP2040-Clay-Printer* has been used to prepare the samples. The printing system (Figure 1a) includes a 3-liter air-tight tank, in which an air-pressurized ram moves the soil toward the extruder; this latter holds an endless screw connected to a stepper motor. The rotation of the screw forces the extrusion of the soil filament through the nozzle. In this work a nozzle with a diameter of $d_n = 1.4$ mm was used. The air pressure in the tank was set to 600 kPa and maintained constant during the whole printing process. The printing velocity has been set equal to 180 mm/min.

The printer was programmed to print samples with a base of 75 mm x 75 mm and a height of 25 mm, obtained by the superposition of horizontal layers. As shown in Figure 1b,

#Corresponding author. E-mail address: marco.rosone@unipa.it
[1]University of Palermo, Department of Engineering, Palermo, Italy.
[2]Ecole Polytechnique Fédérale de Lausanne, Laboratory of Soil Mechanics, Lausanne, Switzerland.

Submitted on May 28, 2022; Final Acceptance on October 7, 2022; Discussions open until February 28, 2023.
https://doi.org/10.28927/SR.2022.005422

Table 1. Main geotechnical properties of the printed soil (specific gravity Gs, liquid limit LL, plastic limit PL, clay fraction fclay, silt fraction fsilt, sand fraction fsand).

Gs (-)	*LL* (-)	*PL* (-)	f_{clay} (%)	f_{silt} (%)	f_{sand} (%)
2.77	0.45	0.21	52	46	2

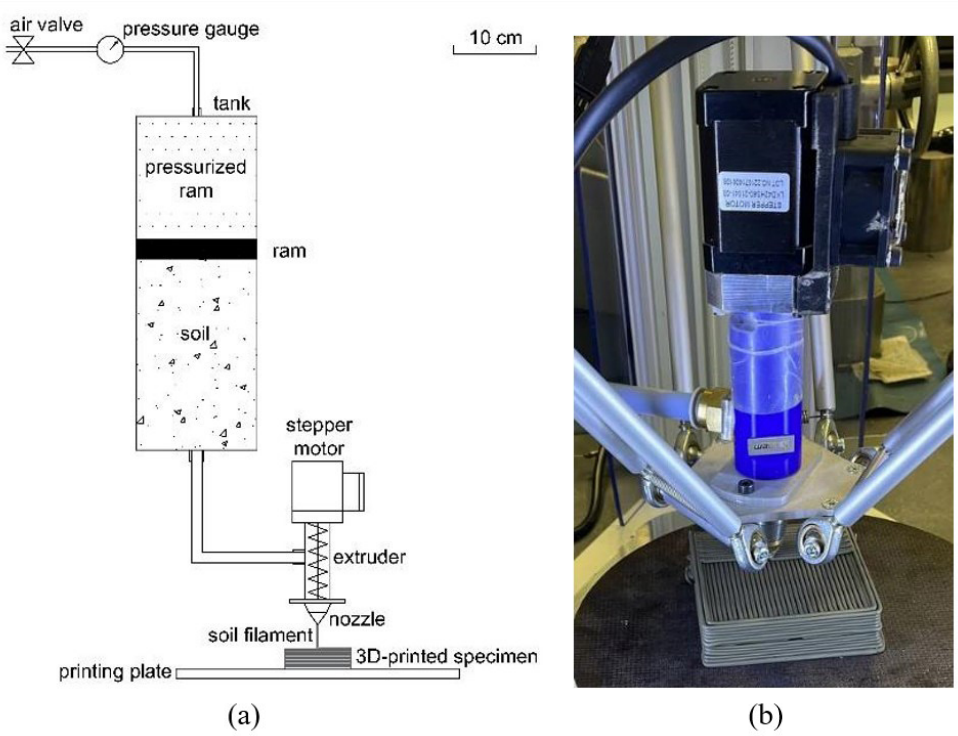

Figure 1. Schematic layout of the 3D soil printer (a) and photo of a sample being printed (b).

each layer was confined with two parallel filaments printed along the perimeter, while the internal part was filled with adjacent filaments extruded along the same direction; in each subsequent layer, the extruding direction was changed by 90 degrees.

Three samples were prepared to assess the repeatability of the printing procedure in terms of final sample characteristics (water content and void ratio). Cubical specimens of around 1 cm^3 were cut from the central part of two printed samples and used for the microstructural investigation.

Scanning Electron Microscope (*SEM*) observations and Mercury Intrusion Porosimetry (*MIP*) tests were carried out on the printed specimens after they were freeze-dried. This operation was done by submerging the specimens in liquid nitrogen (thus creating amorphous ice and avoiding the water volume to increase due to crystallization) and by subsequent sublimation in quasi-vacuum (P = 0.06 mbar) and under low temperature (T = -52°C).

A *Quanta-200-FEG* SEM was used for the observations in high-vacuum mode on golden-coated specimens. *MIP* tests were performed using a porosimeter (*Pascal 140–440 series, Thermo Scientific*) attaining a maximum intrusion pressure of 400 MPa, corresponding to an entrance pore diameter of about 4 nm. An extrusion stage was also performed after the mercury intrusion.

3. Fabric of the printed samples

Water contents of the printed samples were found in a narrow range with an average value of 0.30, slightly lower than the preparation water content, as a probable consequence of a partial consolidation induced by the stress applied through the row, and some drying due to the exposure to atmosphere (measured total suction of as-printed samples was about 0.3 MPa). In spite of some variability in as-printed void ratio (e = 1.07 ± 0.07), the applied 3D-printing procedure was considered adequate to produce samples with similar characteristics. The average degree of saturation was 0.73.

To observe the fabric of the 3D-printed samples, the external surface (top and lateral) and the vertical cross-section of the extracted specimens were observed at *SEM* (Figure 2).

The top surface of the specimen and its cross section are framed at 60X of magnification in Figure 2a and 2b, respectively. In particular, Figure 2a shows a zone of the top surface, where an inversion of the printing direction occurred. At this magnification, the soil filaments appear

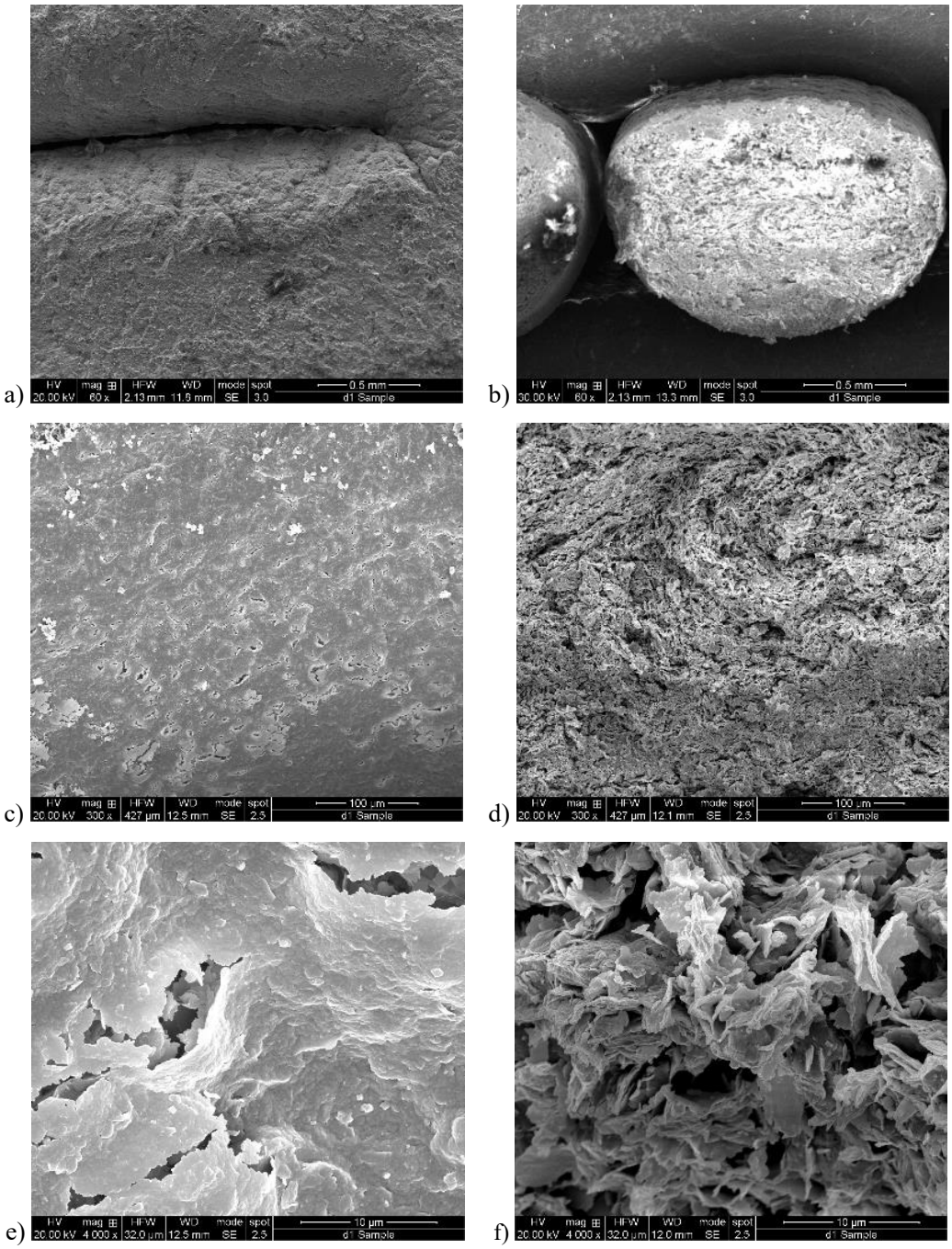

Figure 2. SEM photomicrographs of the 3D-printed soil: external surface (top in a, lateral in c and e) and vertical cross section (b, d and f). Magnifications are 60X (a, b), 300X (c, d) and 4000X (e, f).

homogeneous. Figure 2b shows the result of the superposition of the filaments: a certain ovalization in the cross-section of the filament can be detected, as a probable result of the weight of the above layers. Interestingly, the area of the cross section of the filament coincides with the area of the circle having the diameter of the nozzle (d_n = 1.4 mm), suggesting that the deposition of the filament occurs in undrained conditions, without volume change. As a consequence of this ovalization, a good contact is observed when two filaments overlap, while an inflection is produced in the void space among adjacent filaments. Voids between the soil filaments have an average equivalent diameter of 150 μm and they represent the macropores (inter-filament pores) of the 3D-printed soil.

At 300X, the external surface of the filament (Figure 2c) shows a smooth and compact particle arrangement, with iso-oriented clay particles and few pores 0.3÷1.5 μm wide and 3÷30 μm long. On the microphotograph of the cross-section of the filament at 300X (Figure 2d), a spiral trend of

the particles orientation can be observed, as a result of the rotative movement of the screw in the extruder. Pores having a maximum diameter of about 30 μm as well as pores 1-2 μm wide and 10÷70 μm long can be identified at the contacts between the clay aggregates (Figure 2d).

In the last microphotographs, taken with a 4000X magnification, different arrangements of the clayey particles are visible. Particles on the lateral surface (Figure 2e) are iso-oriented and arranged with face-to-face packing; the arrangement of the particles in the inner part of the filament (Figure 2f) is more complex showing aggregated structures with both face-to-face and edge-to-face contacts. At this magnification, inter-aggregate pores, having a dimension of few microns, and intra-aggregates pores of smaller dimensions (lower than 0.5 μm) are visible. It is worth to observe that where the clayey particles are packed with face-to-face contacts the intra-aggregates pores are smaller.

The results of MIP tests performed on two different specimens are reported in Figure 3a in terms of the intruded/extruded void ratio (e_i, the ratio of the void volume intruded by mercury ($V_{v,i}$) to the volume of soil particles (V_s)) and in Figure 3b in terms of the Pore Side Density *PSD* ($PSD = -\Delta e_i/\Delta(logd)$) as a function of the computed pore diameter d. The total void ratios intruded during the MIP tests (e_i = 0.838 and 0.898) were lower than the mean void ratio measured on the 3D-printed samples (e = 1.07).

This difference is believed to be the result of the pores larger than 120 μm which are filled with mercury before the injection starts, and which are not detected with the technique. This maximum detectable pore diameter well corresponds to the average diameter of the inter-filament pores (150 μm). The intruded void ratio is then attributed to the pores within the filaments only. The corresponding microstructural or intra-filament void ratio (e^m, ratio of the volume of intra-filament pores to the volume of the solid phase) is then quantified in the range of e^m = 0.838÷0.898. The lower bound of macropores, which corresponds to the gaps left by the printing process between the filament, is set to 120 μm (Figure 3).

On the other hand, an analytical evaluation for the macrostructural or inter-filament void ratio (e^M, ratio of the volume of inter-filament pores to the volume of the solid phase) based on geometrical considerations allows to compute a value e^M = 0.274. The sum of the microstructural and macrostructural void ratios is in good agreement with the average void ratio of the 3D-printed samples (Figure 3a, right axis).

The main modal diameter of pores (d = 1 μm, Figure 3b) corresponds both to the pores observed along the external surface of soil filament and to the pores between clayey aggregates observed in the cross-section. According to the procedure proposed by Delage & Lefebvre (1984) intra-assemblage porosity results in a reversible behaviour during the intrusion/extrusion phases, while mercury is trapped by capillary effects in the bigger pores once the applied pressure is removed (Figure 3a). This criterion applied to the two

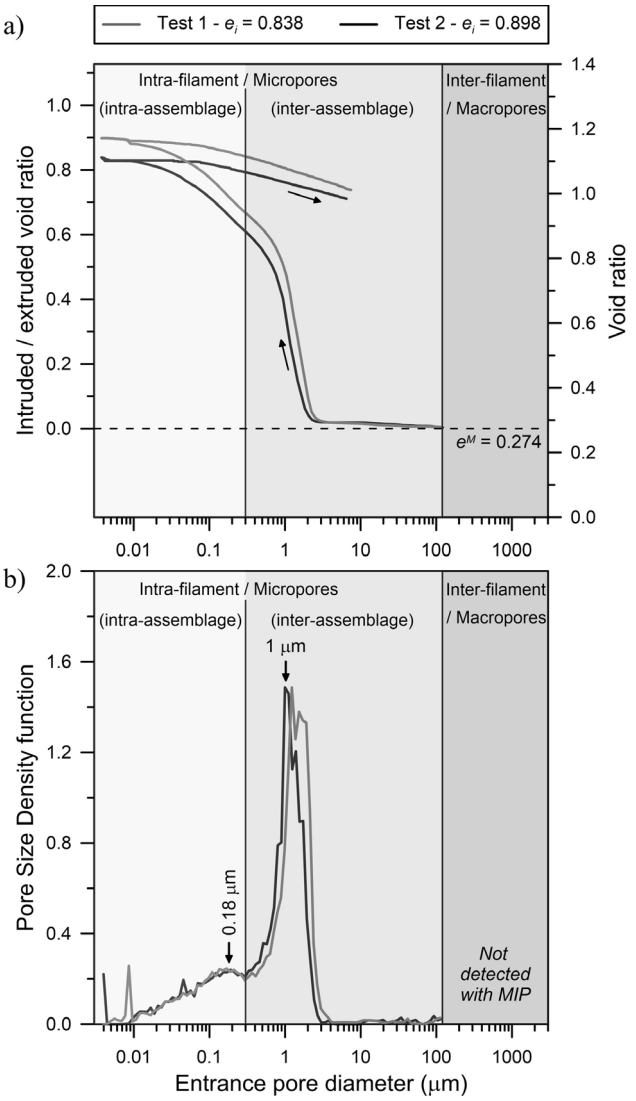

Figure 3. Void ratio (a) and Pore Size Density (b) as a function of the Entrance Pore Diameter from MIP tests.

tests performed could provide the upper bound value of the intra-assemblage as d = 0.127 μm. These micropores include the porosity between clayey particles stacked in face-to-face disposition. However, the criterion based on intrusion and extrusion curves could underestimate the limit value (Yuan et al., 2020). In fact, a secondary peak of *PSD* can be identified in the same range of micropores (d = 0.18 μm). This class of micropores corresponds to the intra-assemblage pores located between particles stacked in face-to-edge disposition (Figure 3f). Then, on the base of *PSD* evolution (Figure 3b) a more consistent upper limit for the intra-assemblage pores domain can be identified at d = 0.3 μm.

4. Conclusion

The note explored the fabric of a 3D-printed clayey soil, highlighting how the particle arrangements and size,

orientation and shape of pores are strongly linked to the printing operation. In particular, it was observed that the macropores are the result of the relative position of the filaments and their initial distortion in quasi-undrained conditions. Particle arrangement within the soil filament is strongly anisotropic due to the rotative movement of the soil in the extruder. Moreover, intra-assemblage pores, located in between the clayey assemblages, and intra-assemblage pores, as the results of different particle contacts (both face-to-face and edge-to-face contacts), characterize the microporosity in the intra-filament soil structure.

It is believed that these observations could pose the basis for engineering the creation of fabric-controlled samples; this capability could serve multiple purposes, such as the production of samples with precise hydro-mechanical characteristics, e.g. permeability and water retention properties.

Declaration of interest

The authors have no conflicts of interest to declare. All co-authors have observed and affirmed the contents of the paper and there is no financial interest to report.

Authors' contributions

Alessio Ferrari: conceptualization, funding acquisition, methodology, supervision, writing, validation. Marco Rosone: conceptualization, methodology, data analysis, writing – original draft. Silvia La Rosa: investigation, formal analysis, writing. Giovanni Sapienza: investigation.

List of symbols

CI consistency index;
d entrance pore diameter in MIP test;
d_n diameter of the nozzle;
e void ratio;
e_i intruded/extruded void ratio in MIP test;
e^m ratio of the volume of intra-filament pores to the volume of the solid phase;
e^M ratio of the volume of inter-filament pores to the volume of the solid phase;
f_{clay} clay fraction;
f_{sand} silt fraction;
f_{silt} silt fraction;
G_s specific gravity;
LL liquid limit;
MIP Mercury Intrusion Porosimetry;
P absolute pressure;
PL plastic limit,
PSD Pore Size Density function from *MIP* test;
SEM Scanning Electron Microscope
T temperature;
V_s volume of soil particles;
$V_{v,i}$ void volume intruded by mercury in *MIP* test;
w water content.

References

Bourke, M.C., Viles, H.A., Nicoli, J., Lyew-Ayee, P., Ghent, R., & Holmlund, J. (2016). Innovative applications of laser scanning and rapid prototype printing to rock breakdown experiments. *Earth Surface Processes and Landforms*, 33, 1614-1621.

Cordão Neto, M.P., Hernandez, O., Reinaledo, R.L., Borges, C., & Caicedo, B. (2018). Study of the relationship between the hydromechanical soil behavior and microstructure of a structured soil. *Earth Sciences Research Journal*, 22(2), 91-101.

Dal Ferro, N., & Morari, F. (2015). From real soils to 3D-printed soils: reproduction of complex pore network at the real size in a silty-loam soil. *Soil Science Society of America Journal*, 79(4), 1008-1017.

Delage, P., & Lefebvre, G. (1984). Study of the structure of a sensitive champlain clay and of its evolution during consolidation. *Canadian Geotechnical Journal*, 21, 21-23.

Ferrari, A., Bosch, J.A., Baryla, P., & Rosone, M. (2022). Volume change response and fabric evolution of granular MX80 bentonite along different hydro-mechanical stress paths. *Acta Geotechnica*, 17, 3719-3730. http://dx.doi.org/10.1007/s11440-022-01481-0.

Gomez, J.S., Chalaturnyk, R.J., & Zambrano-Narvaez, G. (2019). Experimental investigation of the mechanical behavior and permeability of 3D printed sandstone analogues under triaxial conditions. *Transport in Porous Media*, 129, 541-557.

Hanaor, D.A.H., Gan, Y., Revay, M., Airey, D.W., & Einav, I. (2015). 3D printable geomaterials. *Geotechnique*, 66(4), 323-332.

Ju, Y., Xie, H., Zheng, Z., Lu, J., Mao, L., Gao, F., & Peng, R. (2014). Visualization of the complex structure and stress field inside rock by means of 3D printing technology. *Chinese Science Bulletin*, 59(36), 5354-5365.

Khoshnevis, B. (2004). Automated construction by contour crafting – related robotics and information technology. *Automation in Construction*, 13, 5-19.

Mansoori, M., Kalantar, N., & Palmer, W. (2018). Handmade by machine: a study on layered paste deposition methods in 3D printing geometric sculptures. In *Proceedings of the Conference Fabrication and Sculpting Event (FASE) 2018*, Instituto Superior Técnico, Lisbon, Portugal, June 6-8.

Matsumura, S., & Mizutani, T. (2015). 3D printing of soil structure for evaluation of mechanical behavior. Acta Stereologica. In *Proceeding of the 14th International Congress for Stereology and Image Analysis*, Liège, Belgium, July 6-10.

Muñoz-Castelblanco, J.A., Pereira, J.M., Delage, P., & Cui, Y.J. (2012). The water retention properties of a natural unsaturated loess from northern France. *Géotechnique*, 62(2), 95-106.

Perrot, A., Rangeard, D., & Courteille, E. (2018). 3D printing of earth-based materials: processing aspects. *Construction & Building Materials*, 17, 670-676.

Pua, L.M., & Caicedo, B. (2020). Reproducing the inherent variability of soils using a three-dimensional printer. *International Journal of Physical Modelling in Geotechnics*, 21(6), 295-313.

Pua, L.M., Caicedo, B., Castillo, D., & Caro, S. (2018). Development of a 3D clay printer for the preparation of heterogeneous models. In A. McNamara, S. Divall, R. Goodey, N. Taylor, S. Stallebrass & J. Panchal (Eds.), *Physical modelling in geotechnics* (pp. 155-160). CRC Press.

Romero, E., & Simms, P.H. (2008). Microstructure investigation in unsaturated soils: a review with special attention to contribution of mercury intrusion porosimetry and environmental scanning electron microscopy. *Geotechnical and Geological Engineering*, 26, 705-727.

Yuan, S., Liu, X., Romero, E., Delage, P., & Buzzi, O. (2020). Discussion on the separation of macropores and micropores in a compacted expansive clay. *Géotechnique Letters*, 10(3), 454-460.